

# XMM-Newton CCF Release Note

XMM-CCF-REL-358

## EPIC-pn Energy Scale: Long-Term CTI and Quiescent Background Gain Correction

M.J.S. Smith, K. Dennerl, M.J. Freyberg

October 9, 2018

### 1 CCF Components

Name of CCF	VALDATE	EVALDATE	Blocks Changed	CAL Version	XSCS Flag
EPN_CTI_0048.CCF	2000-03-23T05:00:00		LONG_TERM_CTI LTC_TIMES NDSCLIN_GAIN	3.240	NO

### 2 Changes

This release describes the implementation of the time-resolved quiescent-background dependent gain (QBG) correction and associated changes to the long-term CTI (LTCTI) calibration.

Earlier investigations had shown a dependency of the EPIC-pn energy scale on the quiescent particle background (QB) rate. As minimum ionising particles (MIPs) impact the CCD they deposit saturating charge tracks, with the number of saturated pixels per CCD read-out cycle depending on the particle background rate. The total resulting charge shifted to the read-out affects the on-chip analogue amplifier characteristics, which, at such high charge levels, manifests itself as an increase in gain with increasing charge.

Event analysing algorithms are used to identify MIP events and flag associated CCD columns. In nominal operations, for Full Frame (FF), Extended Full Frame (EFF) and Large Window (LW) modes the identification takes place at the on-board data handling level in order to allow removal of the flagged events from the data stream and lower telemetry load. For single CCD read-out modes (Small Window (SW), Timing (TI) and Burst (BU) modes), where the number of recorded MIPS

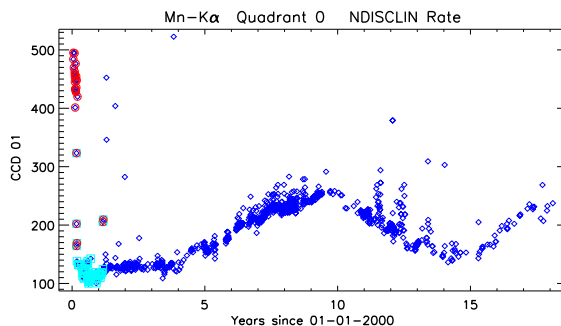


Figure 1: Observation averaged discarded line rates versus time for Quadrant 0 (FF mode). The overall shape of the trend follows the quiescent background level as measured by e.g. the radiation monitor. The nominal MIP detection set-up ( $\text{MAXMIP} == 63$ ,  $\text{MIPSEL} == 5$ ) was used for all but the early epoch of the mission; observations with non-nominal MIP detection set-ups are highlighted as follows:  $\text{MAXMIP} \neq 63$  (red circles),  $\text{MIPSEL} \neq 5$  (magenta squares). Quadrants 1 – 3 show very similar trends.

is smaller and where fast real-time data handling is required, the MIP flagging occurs at the data reduction level in SAS. In either case the number of flagged columns is tracked through the discarded line (DL) counter, which gives the number of flagged columns per 20 CCD frame intervals. There is a strong correlation between the DL counter rate (see Fig. 2) and the quiescent background (as measured by e.g. the radiation monitor), which allows it to be used in the SAS as a proxy for the particle incidence rate.

As part of the time-dependent energy scale correction, the QBG correction has been implemented in SAS in order to account for this behaviour. Since SAS 14, the software already allowed for a correction based on the observation averaged DL rates (although this was not calibrated and a null correction was applied; see Smith et al., 2014). However, subsequent investigations showed that a time-resolved correction was warranted in order to correctly handle varying background levels along an exposure. This has been implemented in SAS 17, and this release describes the associated calibration of the correction. Because there is some dependency of the LTCTI correction on the QBG correction, the calibration of the latter impacts the former. Up to now, the effects of the QB on the gain were partially corrected through the “empirical” LTCTI correction (see e.g. Smith et al. 2010), a method introduced before the effect of the QB on the energy scale was understood. With this release, the LTCTI and QBG corrections have been largely decoupled. For the time-dependent energy scale reconstruction, this yields improvements in:

- high-background observations: the associated gain effects are now better handled;
- spatial accuracy: the LTCTI modelling is less constrained and now better models the measured CTI.

As yet, the QBG correction is calibrated just for FF and EFF modes, as only for these modes sufficient data has been collected over the course of the mission to derive the gain dependency. For LW, SW, TI and BU modes a null QBG correction is applied, and the “empirical” LTCTI correction is maintained.

As mentioned above, the LTCTI and QBG corrections are interdependent and somewhat degen-

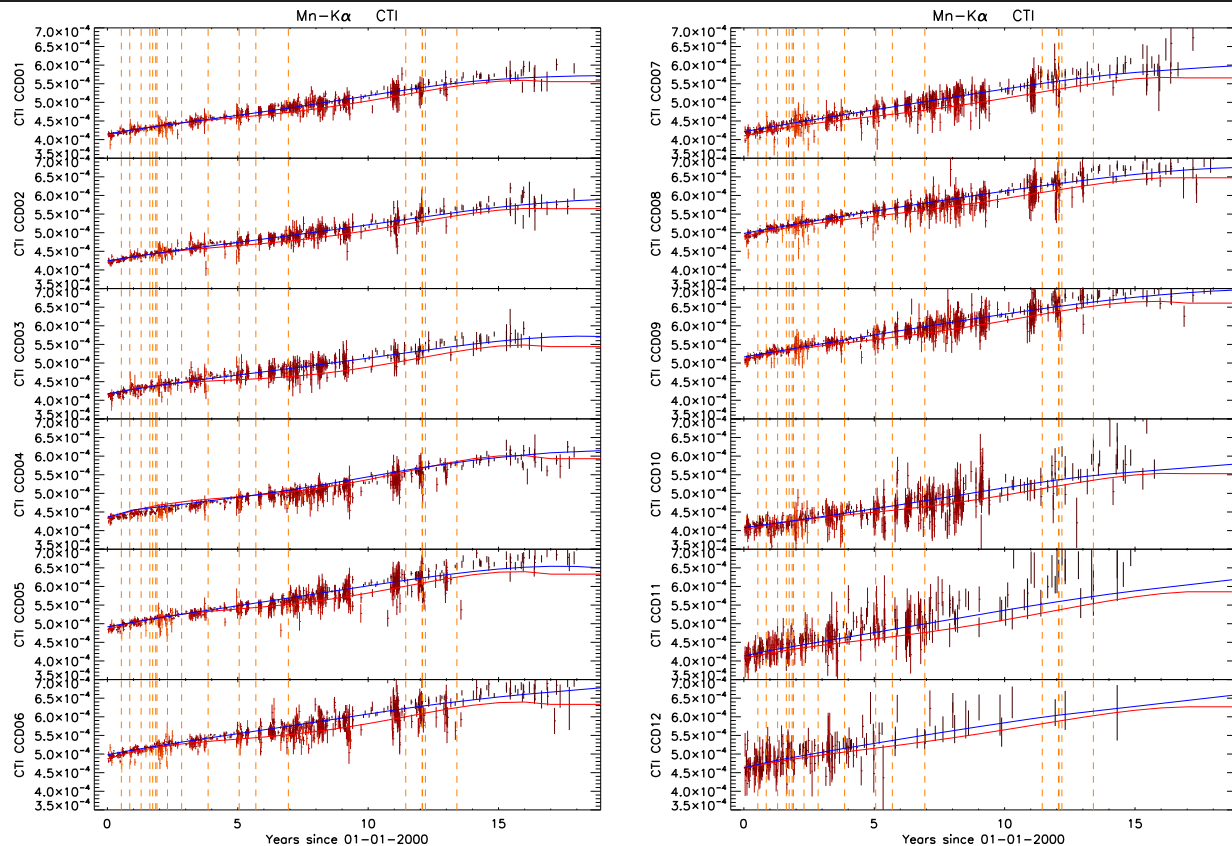


Figure 2: Per CCD, the CTI versus time per as measured at the Mn- $K_{\alpha}$  emission from FF mode *CalClosed* observations. The CTI modelling is overlaid with the old and new CCF in red and blue respectively. Vertical dashed lines indicate times of major solar coronal ejections. The new modelling more closely follows the CTI trend, especially in periods of high quiescent background where the old modelling deviated significantly. Also note that additional deviations of the old modelling are due to extrapolations from May 2016 onwards due to the data available at the time.

erate, especially for later epochs where the data quality is limited due to the natural decay of the on-board calibration source<sup>1</sup>. The respective corrections are derived by iteratively fitting:

1. the measured CTI, with a polynomial (see Sec. 2.1), and
2. the resulting energy scale residuals, with a linear dependency on the DL rate (see Sec. 2.2), until an acceptable convergence is reached.

## 2.1 LTCTI Correction

The LTCTI behaviour is shown in Fig. 2, comparing the modelling used up to now with the new modelling. The deviations from the data of the old LTCTI modelling, especially during epochs of higher quiescent background, have been reduced with the new modelling. Nevertheless, residuals remain, which point to the limitations of the implementation of the long-term energy scale correction. For FF and EFF modes, LTCTI model parameters are derived independently for each CCD, at both Mn- $K_{\alpha}$  as Al- $K_{\alpha}$  energies. Owing to the remaining residuals in the CTI modelling, for CCD 4 the

<sup>1</sup>Data are obtained from *CalClosed* observations, using single events with no precursors. Energies are corrected for out-of-time events, and spatial selection is limited to regions of sufficiently low out-of-time fractions.

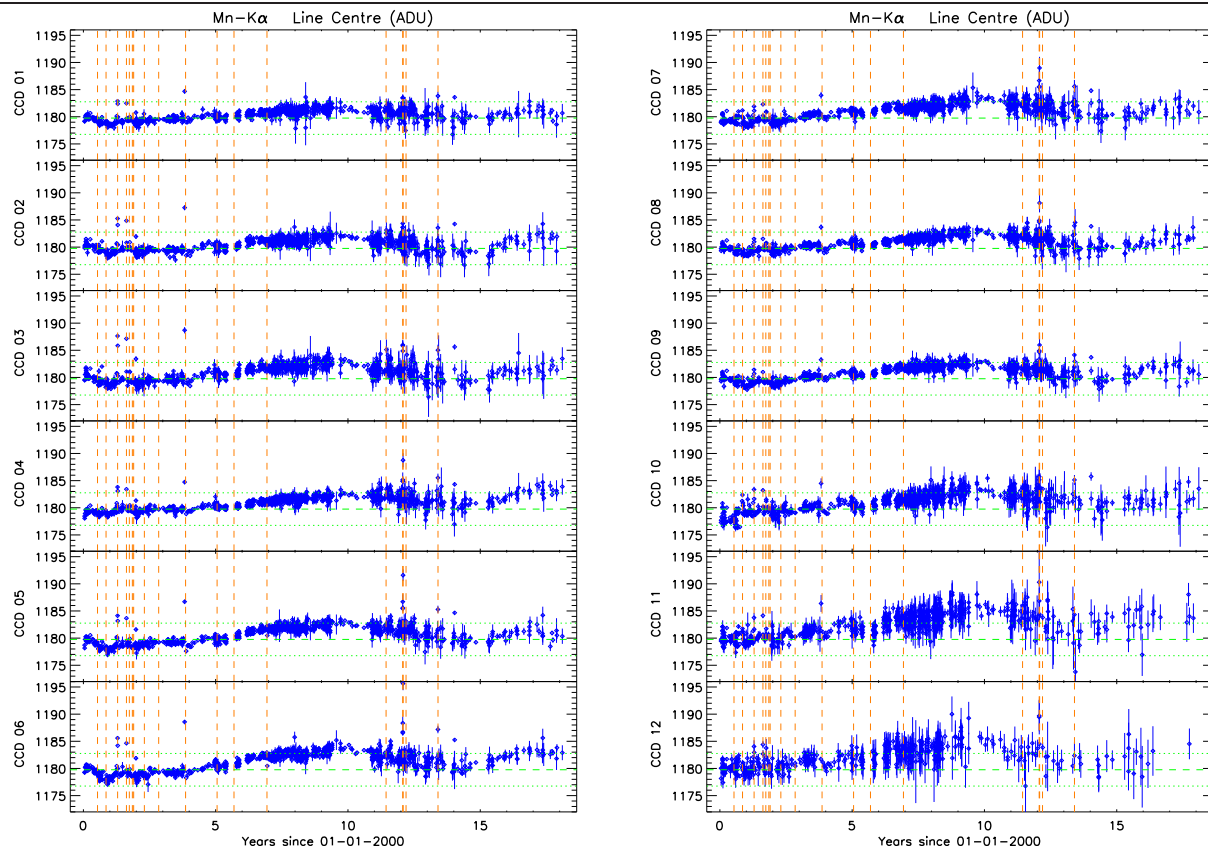


Figure 3: Per CCD, the reconstructed Mn-K $\alpha$  line energies versus time, using the latest CTI modelling, and without applying the QBG correction. The horizontal green dashed line shows the nominal line energy, with the  $\pm 3$  ADU range indicated by the green dotted lines. There are clear long-term deviations from the laboratory energy, which are due to the QBG.

model is derived from data obtained from an area around the boresight (RAWY in [181:200]) in order to optimise the energy reconstruction for targeted sources.

The respective LTCTI model parameters are tabulated in the LONG\_TERM\_CTU and LTC\_TIMES extensions.

## 2.2 QBG Correction

Fig. 3 shows the energy reconstruction obtained with the new LTCTI correction<sup>2</sup>. As expected, large-scale long-term effects have been corrected. However, significant over-corrections are evident, both in individual observations as in an overall trend, which are a result of the QBG. A linear correlation between the resulting energies and the observation averaged DL rates versus time (see Fig. 4, left panel) yields the QBG correction parameters. Similarly to the LTCTI correction, the QBG model parameters are derived independently for each CCD, although at Mn-K $\alpha$  energies only. The resulting model well describes the (much weaker) QBG at Al-K $\alpha$  energies (see Fig. 4, right panel).

<sup>2</sup>Unless otherwise stated, energies are given in units of ADU (= 5 eV)

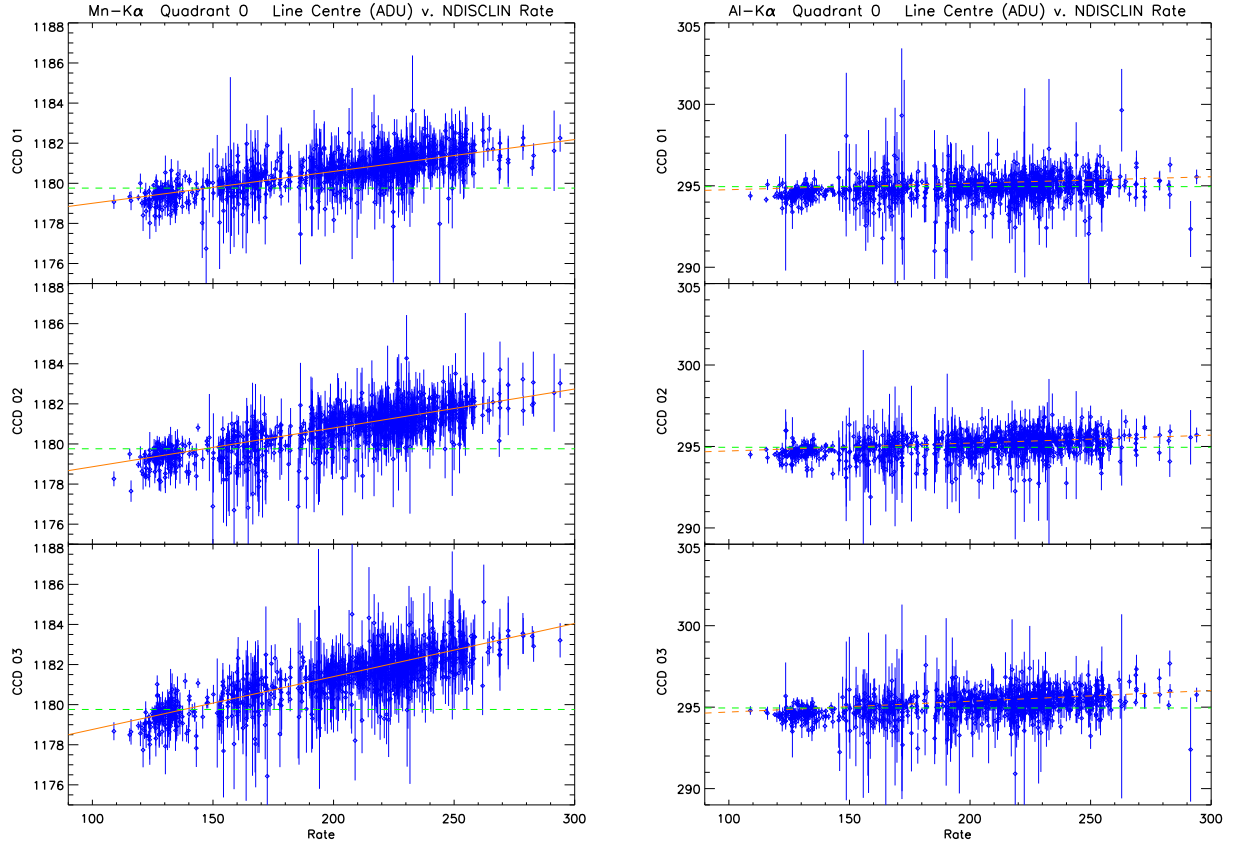


Figure 4: Reconstructed energy versus observation averaged discarded line rate at Mn- $K_{\alpha}$  (*left panel*) and Al- $K_{\alpha}$  (*right panel*) for Quadrant 0 CCDs (FF mode). The energies shown here are determined in the same way as those in Fig. 3, i.e. using the latest LTCTI correction. A linear fit to the Mn- $K_{\alpha}$  data is shown in the solid red line in the left panel. The red dotted line in the right panel shows the same fit gain scaled to the Al- $K_{\alpha}$  energy. Quadrants 1 – 3 show similar trends.

The calibration values are contained in the `OFFSET` and `SLOPE` columns of the `NDSCLIN_GAIN` extension.

A complication arises in the early phase of the mission due to differing parameters of the MIP identification algorithm which strongly affect the relationship between MIP and DL rates. This is summarized below:

Parameter	Nominal value	Non-nominal value	Calibrated
MAXMIP	63	mainly 5; used up to rev. 52	No (MAXMIP5C keyword placeholder)
MIPSEL	1	mainly 2; used up to rev. 228	Yes (MIPSEL2C keyword)

Owing to the uncalibrated status of observations with  $\text{MAXMIP} \neq 63$ , the QBG correction (and associated LTCTI modelling) is only applied from revolution 53 onwards. Observations in earlier revolutions fall back to the combination of old LTCTI correction and null QBG correction. This is implemented through the `VALIDATE` keyword of the new CCF.

### 3 Scientific Impact and Estimated Quality

Figs. 5 to 10 show comparisons of old versus new energy reconstruction per CCD for FF and EFF modes. In terms of overall trend, the changes between old and new calibration are minor, and are mainly due to the inclusion of more recent data in the new LTCTI modelling. However, the main differences are seen for a set of individual observations at Mn-K $_{\alpha}$ , where the implementation of the QBG correction yields substantial improvements. To better illustrate the impact, observations with large discrepancies between reconstructed and laboratory energies are marked in red (Figs. 6 and 9). In almost all such cases, the new calibration yields significantly better results, evidenced by the reduced discrepancies between reconstructed and expected energy. This is further illustrated in Fig 11, which shows, per CCD, the distribution of differences of new with respect to old calibration in terms of absolute deviation from the expected energy, i.e.:  $|E_{new} - E_{lab}| - |E_{old} - E_{lab}|$ . For most CCDs, the distributions are skewed to negative values, indicating an improvement with the new calibration.

Nevertheless, in the set of *CalClosed* data there are two observations where the opposite is the case (ObsIds 0134520501 and 0148742501 in 04/2001 and 10/2003 respectively). Both observations were subject to extremely high particle background incidence with DL rates of 450 - 700 s $^{-1}$ , compared to the typical range of 100 - 300 s $^{-1}$ . Due to the non-linearity of the QBG towards very high QB levels, in these cases the gain is significantly over-corrected. In practice, however, similar cases would trigger radiation alerts, and the amount of science data collected under such conditions would be limited.

The impact of the new LTCTI modelling on the spatial accuracy of the energy scale has also been investigated in terms of the variance of reconstructed Mn-K $_{\alpha}$  line energies determined from data obtained from up to ten adjacent spatial regions along the read-out direction. Results are given in Fig. 12, which shows the difference in variance obtained with the new with respect to the old calibration, versus time. Owing to the limited counts per region, the statistical quality of these results is reduced and data have been binned for clarity. Also note that, due to the inhomogeneous illumination of the calibration source, there is insufficient data for CCDs 11 and 12. For most CCDs, there is a clearly reduced variance in line energy for the new calibration in epochs of high QB. This is because, especially in these periods, the old LTCTI modelling deviated from the measured CTI trend to partially correct for the QBG.

The importance of the time-resolved implementation of the QBG correction is illustrated in Fig. 13. This example shows an observation with significant variation of the DL rate along the exposure, and the resulting reconstructed energies using different time bins to determine the event-wise QBG correction. In addition, the results of the “empirical” LTCTI correction, and that of the non-time resolved QBG correction are shown; these yield an energy overcorrection and undercorrection, respectively. More accurate results are obtained with higher temporal resolutions. In the SAS, a default time bin of 100 sec has been implemented. The choice is based on a compromise between sufficiently high temporal resolution, limiting the impact of the intrinsic noise of the DL data on the energy resolution, and robustness against DL data gaps and outliers.

A summary of the accuracy of the *CalClosed* energy reconstruction obtained with the QBG correction and new LTCTI modelling is given in Table 1.

Mode	Pattern	$\overline{E}_{measured} - E_{nominal}$ (eV)	
		Al-K $_{\alpha}$ ( $E_{nominal} = 1.486$ keV)	Mn-K $_{\alpha 2}$ ( $E_{nominal} = 5.888$ keV)
FF	singles	$-1.7 <3.7> (-1.1 <2.9>)$	$-0.9 <2.9> (-1.0 <3.2>)$
	doubles	$-4.2 <5.8> (-2.3 <4.6>)$	$+5.4 <8.4> (+7.3 <5.8>)$
EFF	singles	$-1.7 <3.6> (-1.1 <3.6>)$	$-1.5 <4.2> (-1.2 <3.7>)$
	doubles	$-1.5 <6.2> (-0.1 <7.3>)$	$+2.1 <4.4> (+3.7 <4.8>)$

Table 1: Summary of the EPIC-pn energy reconstruction accuracy at the boresight location for *CalClosed* observations taken over the course of the mission. Values shown are the mean and standard deviation (in eV) of the differences between measured line centroid and nominal energy. They are derived from all observations with exposure times  $\geq 10$  ks since launch; values between parentheses exclude observations taken before 2002.



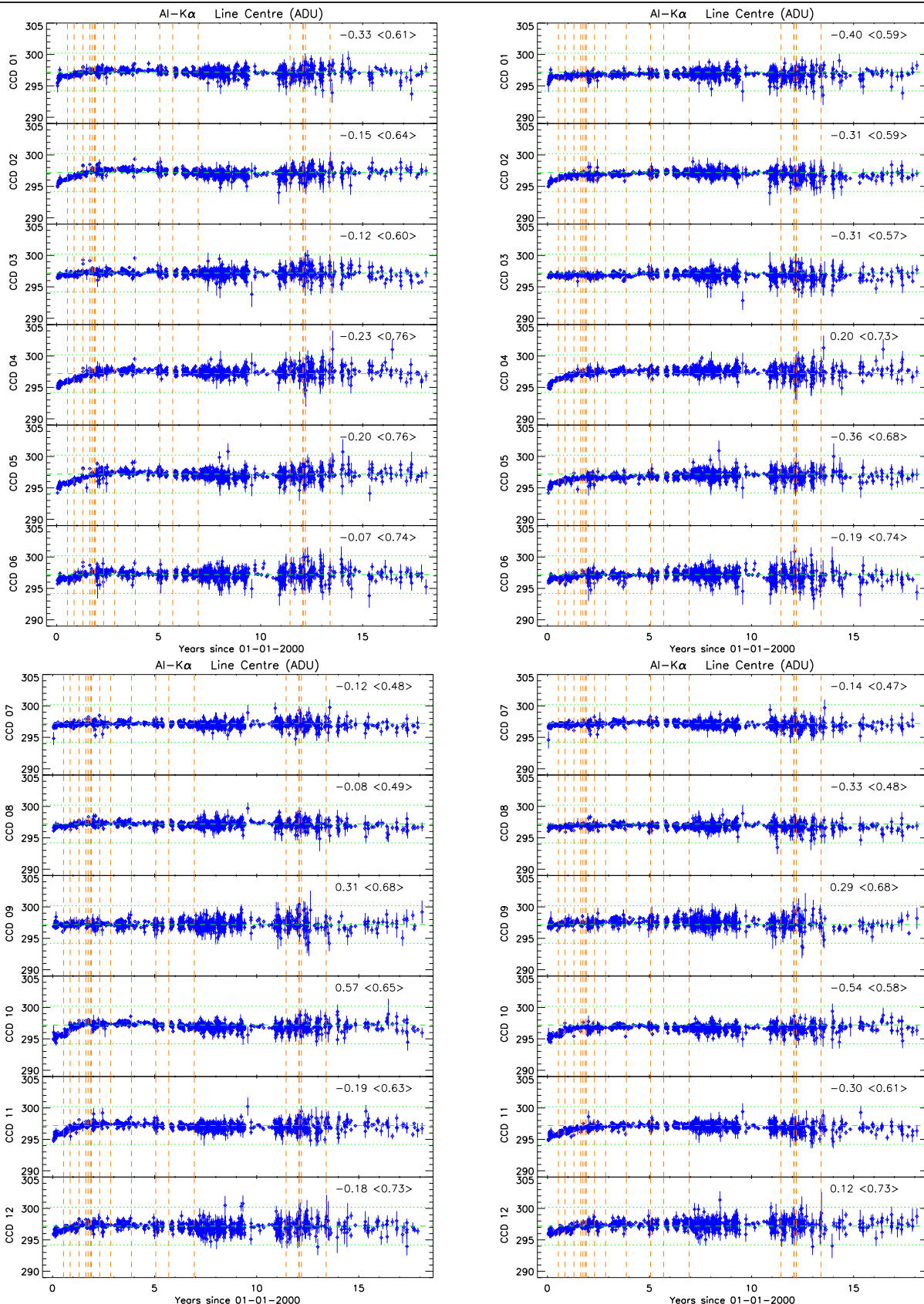


Figure 5: Comparison of the Al-K $\alpha$  reconstructed line centroid energies (in ADU) as determined from FF mode *CalClosed* observations using the old (*left panels*) and new (*right panels*) long-term CTI calibration. The data shown here are based on first-single events extracted from the well illuminated areas of the complete CCDs. The nominal line energy and the  $\pm 3$  ADU margin are shown by the green dashed and dotted lines, respectively; the vertical dashed lines indicate the times of major solar coronal mass ejections. Per CCD, the sample mean and standard deviation are indicated.



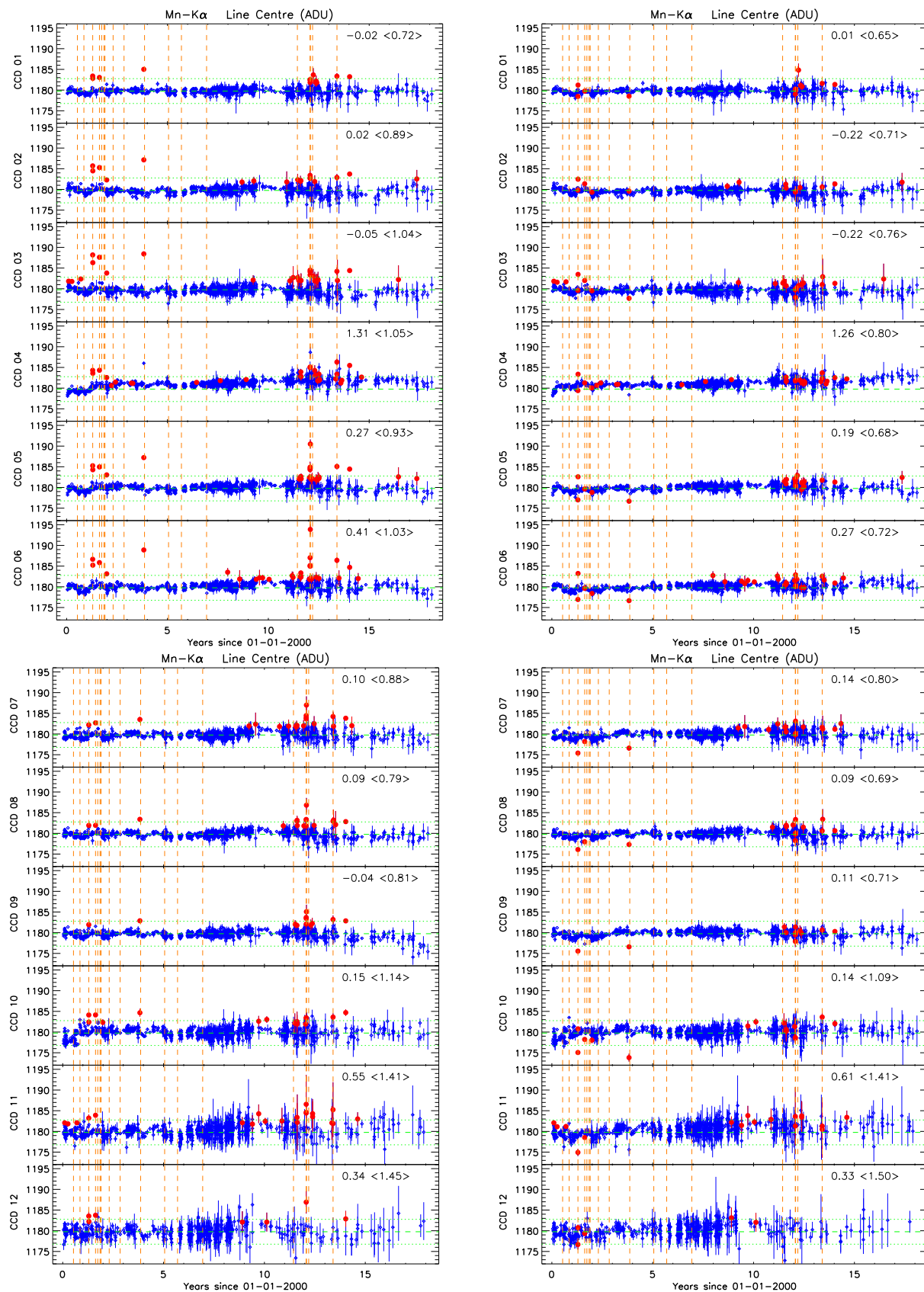


Figure 6: As Fig 5, for FF mode at Mn-K $\alpha$ . Observations with large discrepancies in reconstructed energy in the old calibration are indicated with red data points.

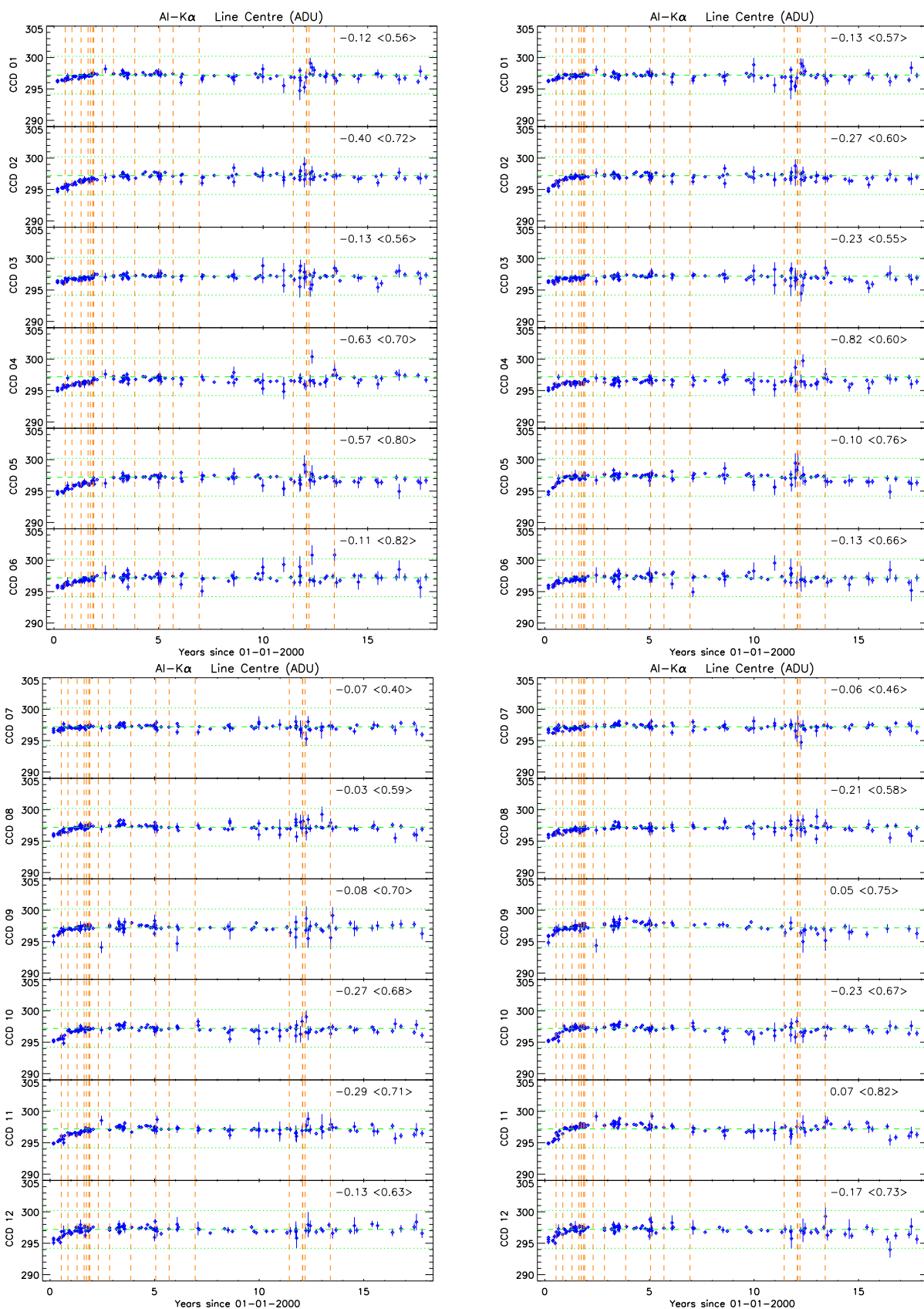


Figure 7: As Fig 5, for EFF mode at Al-K $\alpha$ .

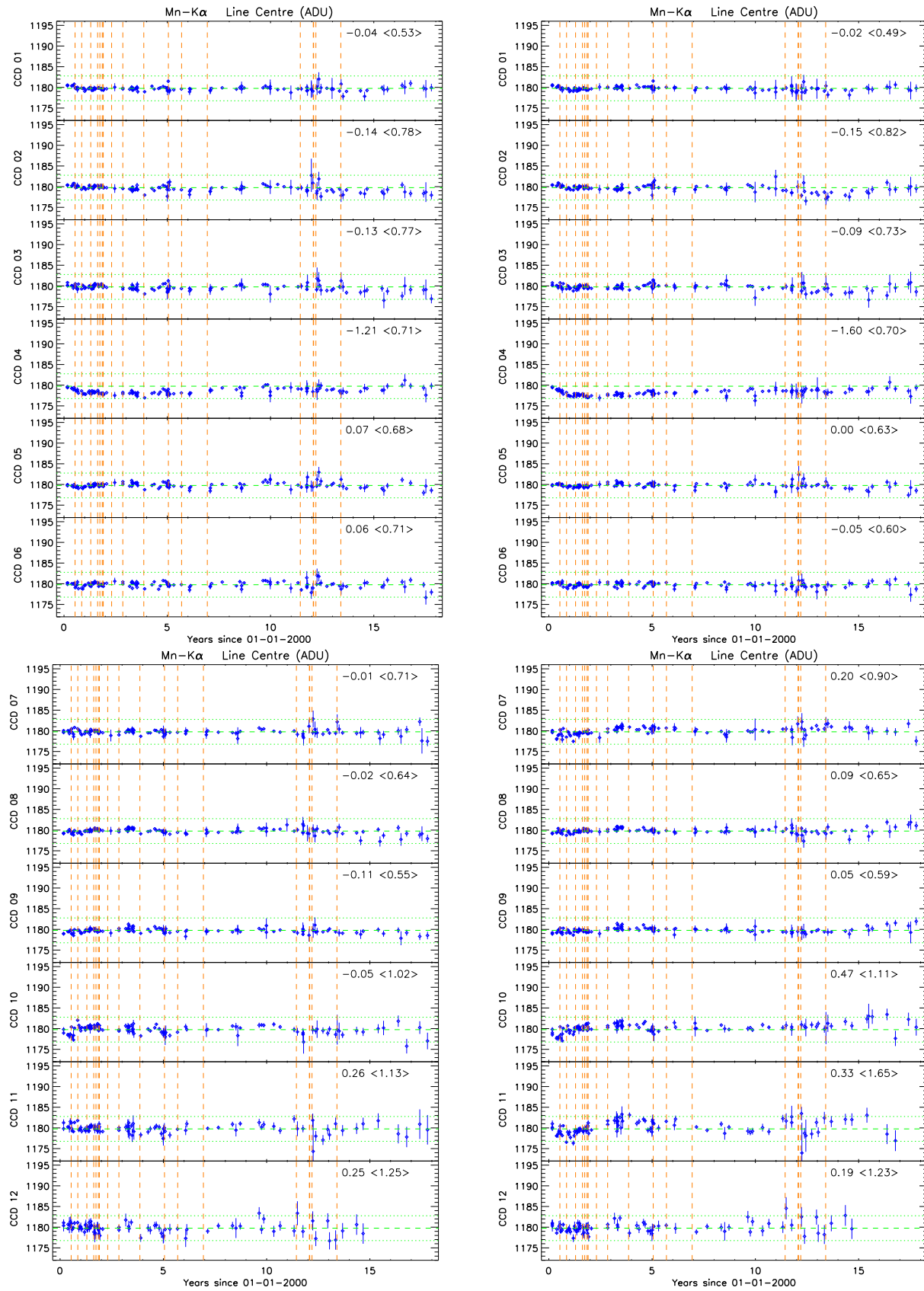


Figure 8: As Fig 7, for EFF mode at Mn-K $\alpha$ .

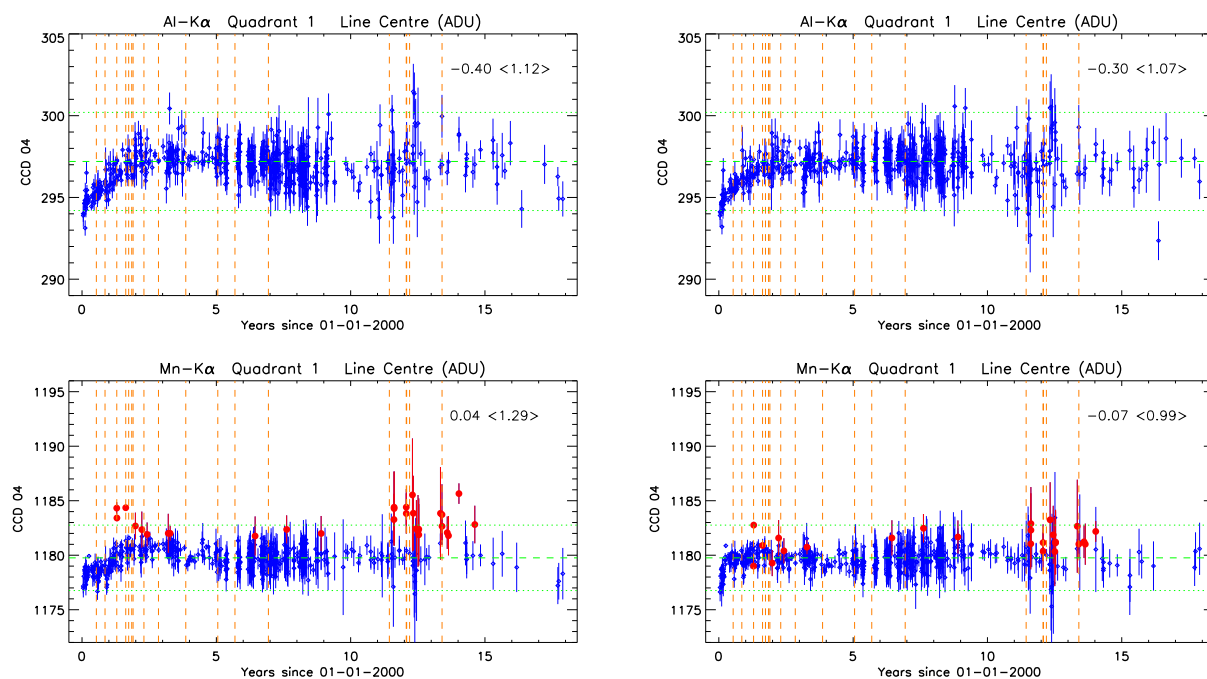


Figure 9: As Figs. 5 and 6, but for data taken from a 20-row region around the boresight. Top row: FF mode at Al-K $\alpha$ , bottom row: FF mode at Mn-K $\alpha$ .

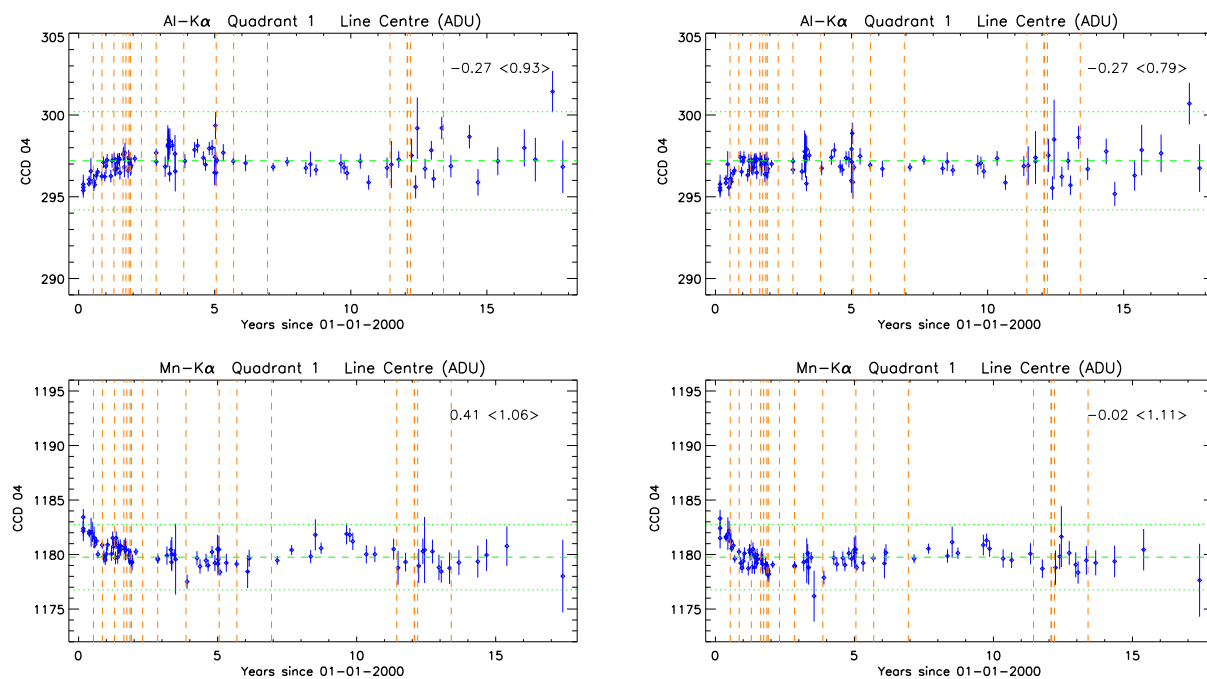


Figure 10: As Fig 9, for EFF mode data. Top row: Al-K $\alpha$ , bottom row: Mn-K $\alpha$ .

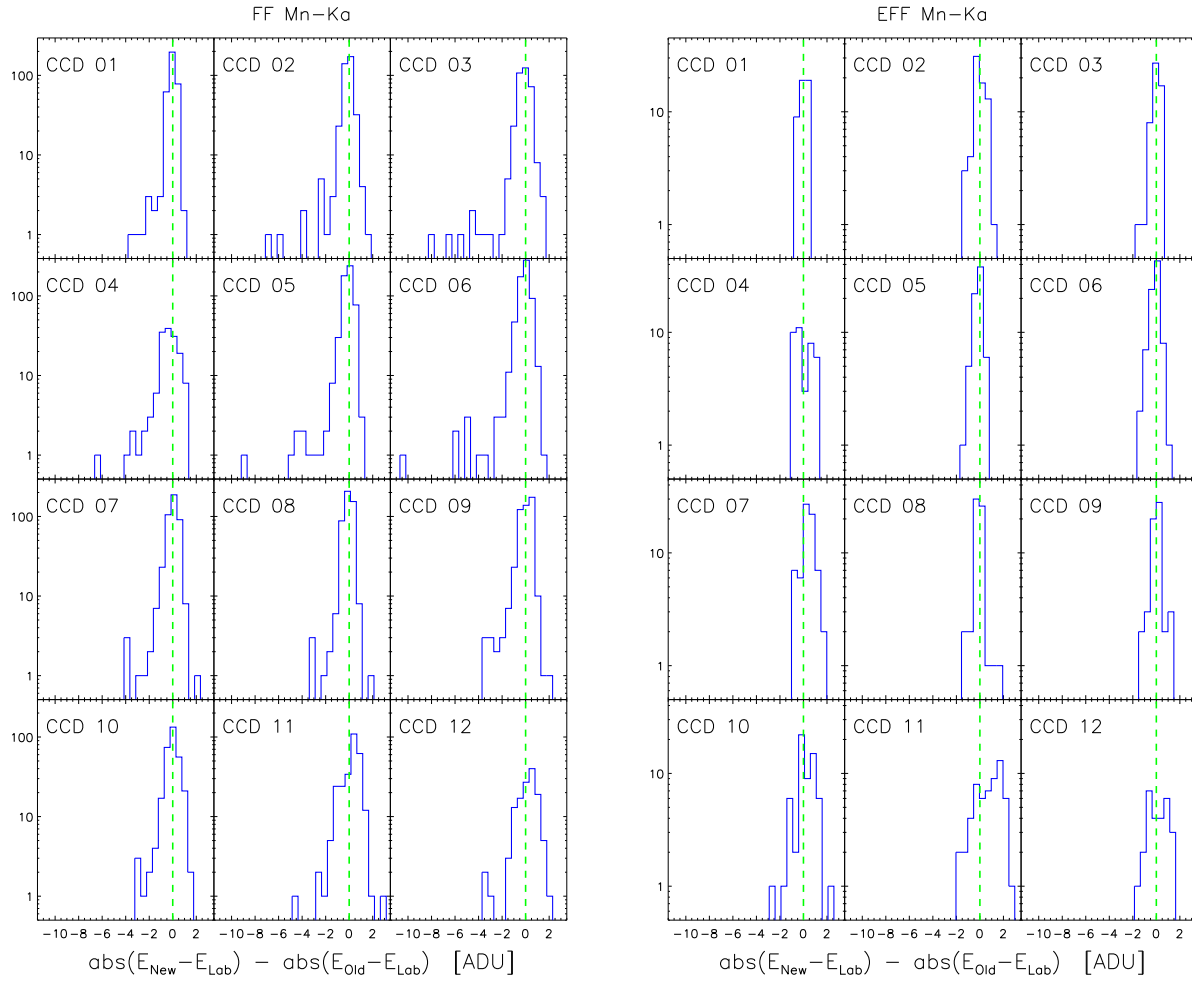


Figure 11: Per CCD, distribution of absolute differences between reconstructed and laboratory energies for the new calibration with respect to the old calibration, at Mn- $K_{\alpha}$ . *Left panel:* FF mode observations; *right panel:* EFF mode observations.

## 4 Test Procedures

Verification of functionality of EPN\_CTL0048.CCF with SAS 17.0: `calview`, `cifbuild`, `epproc`, `epchain`.

## 5 Expected Updates

As the PN LTCTI will continue to develop in time, model parameters will have to be periodically updated. Inclusion of an extra LTCTI calibration point based on the Cu- $K_{\alpha}$  fluorescent emission line is under investigation.

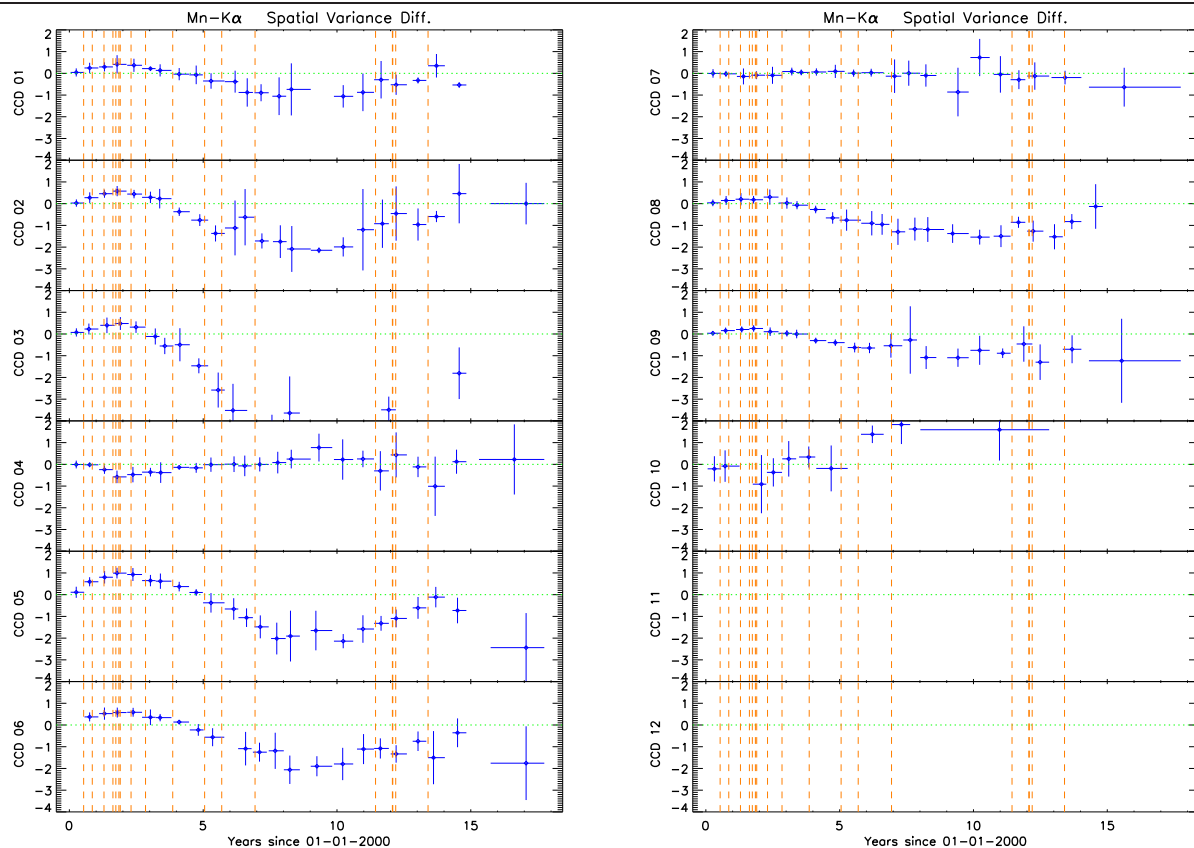


Figure 12: Per CCD, spatial consistency of the energy reconstruction (at  $\text{Mn-K}\alpha$  for FF mode) in terms of the variance of line energies obtained in ten 20-RAWY-wide segments along each respective CCD. The difference between new and old variance is shown versus time; data are binned for clarity. The new calibrations yields a reduced variance, especially where the old empirical CTI correction was adjusted to correct for the high-background related gain. CCD 4 shows no significant improvement because both the old and new calibration is optimised for the boresight region. Note there is insufficient data for CCDs 11 and 12.

## 6 References

Smith, M.J.S., et al., 2010, XMM-SOC-CAL-SRN-0271

(<http://xmm2.esac.esa.int/docs/documents/CAL-SRN-0271-1-0.ps.gz>)

Smith, M.J.S., et al., 2014, XMM-SOC-CAL-SRN-0323

(<http://xmm2.esac.esa.int/docs/documents/CAL-SRN-0323-1-1.ps.gz>)

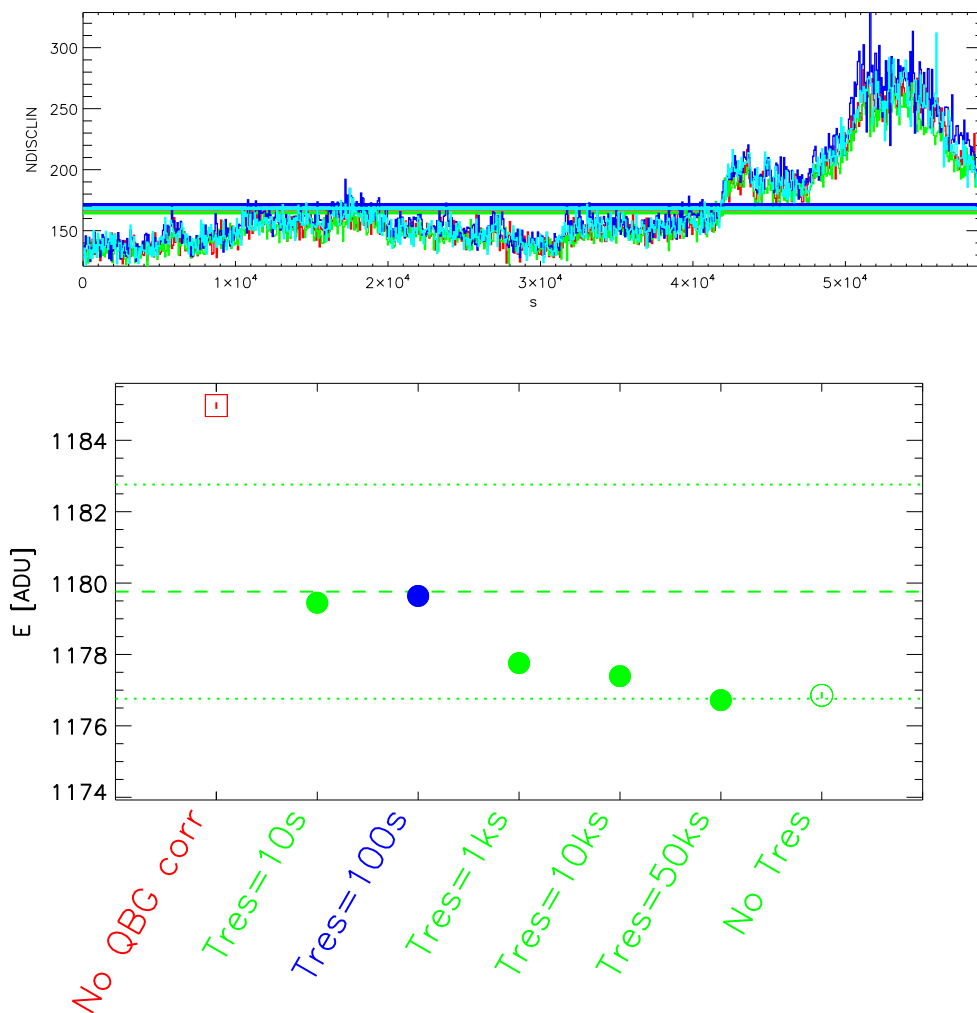


Figure 13: Example of the impact of the temporal binning on the time resolved QBG correction for an observation with significant variation of DL rate (ObsId 0068940101, FF mode, at Mn- $K_{\alpha}$ ). *Top panel*: DL rate (different colours per quadrant) versus time along the exposure; the observation averaged DL rates are indicated with the horizontal lines. *Bottom panel*: Reconstructed energy for different correction methods, coded as follows: *open square*: no QBG correction applied; *solid circles*: time-resolved QBG correction using various DL rate bin sizes; *open circle*: QBG using observation averaged DL rate. The blue point indicates the result obtained with the default DL rate binning of 100 sec.